Inorg. Chem. **2005**, *44*, 502–511

Inorganic Chemistry
Article

Single-Molecule Magnets: Structure and Properties of $[Mn_{18}O_{14}(O_2CMe)_{18}(hep)_4(hepH)_2(H_2O)_2](ClO_4)_2$ with Spin $S = 13$

E. K. Brechin,[†] E. C. Sañudo,[†,‡] W. Wernsdorfer,[§] C. Boskovic,[†] J. Yoo,[||] D. N. Hendrickson,[||] A. Yamaguchi,[⊥] H. Ishimoto,[⊥] T. E. Concolino,[⊗] A. L. Rheingold,[⊗,○] and G. Christou*,[†,‡]

Department of Chemistry, Indiana University, Bloomington, Indiana 47405, Department of Chemistry, University of Florida, Gainesville, Florida 32611, Laboratoire Louis Néel-CNRS, BP 166, 25 Avenue des Martyrs, 38042, Grenoble, Cedex 9, France, Department of Chemistry and Biochemistry, University of California at San Diego, La Jolla, California 92093, Institute for Solid State Physics, University of Tokyo, 5-1-5 Kashiwanoha, Kashiwa, 277-8581 Chiba, Japan, and Department of Chemistry, University of Delaware, Newark, Delaware 19716

Received August 18, 2004

The reaction of 2-(hydroxyethyl)pyridine (hepH) with a 2:1 molar mixture of $[Mn_3O(O_2CMe)_6(py)_3]ClO_4$ and $[Mn_3O(O_2CMe)_6(py)_3]$ in MeCN afforded the new mixed-valent ($16Mn^{III}$, $2Mn^{II}$), octadecanuclear complex $[Mn_{18}O_{14}(O_2CMe)_{18}(hep)_4(hepH)_2(H_2O)_2](ClO_4)_2$ (**1**) in 20% yield. Complex **1** crystallizes in the triclinic space group $P\bar{1}$. Direct current magnetic susceptibility studies in a 1.0 T field in the 5.0–300 K range, and variable-temperature variable-field dc magnetization studies in the 2.0–4.0 K and 2.0–5.0 T ranges were obtained on polycrystalline samples. Fitting of magnetization data established that complex **1** possesses a ground-state spin of $S = 13$ and $D = -0.18$ K. This was confirmed by the value of the in-phase ac magnetic susceptibility signal. Below 3 K, the complex exhibits a frequency-dependent drop in the in-phase signal, and a concomitant increase in the out-of-phase signal, consistent with slow magnetization relaxation on the ac time scale. This suggests the complex is a single-molecule magnet (SMM), and this was confirmed by hysteresis loops below 1 K in magnetization versus dc field sweeps on a single crystal. Alternating current and direct current magnetization data were combined to yield an Arrhenius plot from which was obtained the effective barrier (U_{eff}) for magnetization reversal of 21.3 K. Below 0.2 K, the relaxation becomes temperature-independent, consistent with relaxation only by quantum tunneling of the magnetization (QTM) through the anisotropy barrier via the lowest-energy $M_S = \pm 13$ levels of the $S = 13$ spin manifold. Complex **1** is thus the SMM with the largest ground-state spin to display QTM.

Introduction

There are many specialized applications of magnets that require monodisperse, nanoscale magnetic particles, and the discovery that individual molecules can function as nanoscale magnets was thus a significant development[1–3] for the field of magnetism and magnetic materials. Such molecules have since been named single-molecule magnets (SMMs). SMMs function as single domain magnetic particles that, below their blocking temperature (T_B), exhibit the classical property of a magnet, namely magnetization hysteresis. In addition, SMMs straddle the classical/quantum interface in also displaying quantum tunneling of magnetization (QTM)[4] and quantum phase interference.[5] An SMM derives its unusual properties from a combination of large spin (S) and large, easy axis-type anisotropy (negative axial zero-field splitting parameter D). These result in a significant barrier to thermally

---

* Address correspondence to this author. E-mail: christou@chem.ufl.edu.

[†] Indiana University.

[‡] University of Florida.

[§] Laboratoire Louis Néel-CNRS.

[||] University of California.

[⊥] University of Tokyo.

[⊗] University of Delaware.

[○] Present address: University of California.

(1) Christou, G.; Gatteschi, D.; Hendrickson, D. N.; Sessoli, R. *MRS Bull.* **2000**, *25*, 67.

(2) Sessoli, R.; Tsai, H. L.; Schake, A. R.; Wang, S.; Vincent, J. B.; Folting, K.; Gatteschi, D.; Christou, G.; Hendrickson, D. N. *J. Am. Chem. Soc.* **1993**, *115*, 1804.

(3) Sessoli, R.; Gatteschi, D.; Caneschi, A.; Novak, M. A. *Nature* **1993**, *365*, 141.

(4) Friedman, J. R.; Sarachik, M. P. Tejada, J.; Ziolo, R. *Phys. Rev. Lett.* **1996**, *76*, 3830.

(5) Wernsdorfer, W.; Sessoli, R. *Science* **2000**, 2417.

10.1021/ic048857a CCC: $30.25

activated magnetization relaxation, with upper limits given by $S^2|D|$ or $(S^2 - {}^1/_4)|D|$ for integer and half-integer spin, respectively. The first SMM was $[Mn_{12}O_{12}(O_2CMe)_{16}(H_2O)_4]$,[1-3] with $S = 10$ and $D = -0.50$ cm^{-1} $= -0.72$ K. Since then, other oxidation levels of the $[Mn_{12}]$ family,[6,7] and other Mn_x and M_x (M = Fe, V, Ni) SMMs have been prepared with various S values, both integer and half-integer.[8-11]

Recently, the first exchange-coupled dimer of SMMs has demonstrated the feasibility of fine-tuning the quantum properties of these nanoscale magnetic materials.[12] Most known SMMs contain Mn(III). This is due to the combination of a large number of unpaired electrons on each high-spin, near-octahedral Mn(III) ion and the Jahn–Teller (JT) distortion that accompanies it, usually in the form of an axial elongation.[13] The JT distortion results in a significant magnetoanisotropy, as gauged by the zero-field splitting (ZFS) parameter D, which is always negative for axially elongated Mn, stabilizing the largest value of M_S and giving rise to a uniaxial barrier for the relaxation of the magnetization, i.e., Ising or easy-axis anisotropy.

The nanoscale dimensions of SMMs place them at the quantum/classical interface, and the phenomenon of quantum tunneling of the magnetization (QTM) can be observed as steps in the hysteresis loops. Additionally, QTM within the ground-state (i.e. lowest energy) M_S levels can be observed as temperature-independent relaxation at low enough temperatures. This has been observed for several SMMs.[8a,d,12,14,15]

We have a long-standing interest in the synthesis of Mn clusters with large ground-state spin values that can function as SMMs, and have in the past developed Mn cluster chemistry with a variety of chelating ligands, such as bipyridine (bpy), picolinate (pic$^-$), and the anion of dibenzoylmethane (dbm$^-$), among others.[16] Most of these ligands have one strongly preferred binding mode to the metals, usually chelating one metal. A more flexible ligand, however, is the anion of 2-(hydroxyethyl)pyridine (hepH), which can adopt a variety of possible binding modes, including bridging two, three, or four metals in a variety of fashions, and thus can foster high nuclearity metal clusters with various M_x topologies. In this work, we report the synthesis and magnetic properties of the new mixed valent $Mn(II)_2Mn(III)_{16}$ complex, $[Mn_{18}O_{14}(O_2CMe)_{18}(hep)_4(hepH)_2(H_2O)_2](ClO_4)_2$ (**1**). A preliminary communication of this work has appeared.[17]

Experimental Section

All manipulations were performed under aerobic conditions, using materials as received. $[Mn_3O(O_2CMe)_6(py)_3](ClO_4)$ and $[Mn_3O(O_2CMe)_6(py)_3]$ were prepared as previously described.[18]

$[Mn_{18}O_{14}(O_2CMe)_{18}(hep)_4(hepH)_2(H_2O)_2](ClO_4)_2$ (1). To a solution of $[Mn_3O(O_2CMe)_6(py)_3](ClO_4)$ (0.50 g, 0.57 mmol) and $[Mn_3O(O_2CMe)_6(py)_3]\cdot py$ (0.24 g, 0.29 mmol) in MeCN (40 mL) was added hepH (0.16 g, 1.30 mmol). The resulting solution was stirred overnight, filtered through Celite, and layered with two volumes of Et_2O. After several weeks, the crystals that had formed were isolated by filtration, washed with Et_2O, and dried in vacuo; yield 20%. A sample for crystallography was kept in contact with the mother liquor to prevent interstitial solvent loss. The vacuum-dried sample analyzed as unsolvated. Anal. Calcd (Found) for $[Mn_{18}O_{14}(O_2CMe)_{18}(hep)_4(hepH)_2(H_2O)_2](ClO_4)_2$ (**1**): C 28.87 (29.00); H 3.35 (3.25); N 2.59 (2.61)%. Selected IR data (KBr disk, cm^{-1}): 1577 (vs), 1485 (m), 1442 (s), 1398 (s), 1334 (m), 1248 (w), 1107 (s), 1089 (s), 1070 (s), 1032 (s), 939 (s), 873 (w), 769 (m), 711 (m), 663 (s), 625 (s), 588 (s).

Physical Methods. Infrared spectra (KBr disk) were recorded on a Nicolet NEXUS 670 spectrometer. Elemental analyses were performed by Atlantic Microlab, Inc., Norcross, GA, or at the in-house facility at the Department of Chemistry, University of Florida. Variable-temperature magnetic susceptibility data were collected on powdered microcrystalline samples (restrained in eicosane to prevent torquing) with a Quantum Design MPMS-XL SQUID magnetometer equipped with a 5 T magnet. Pascal's constants were used to estimate the diamagnetic correction, which was subtracted from the experimental susceptibility to give the molar magnetic susceptibility (χ_M). Magnetization versus field hysteresis and dc decay measurements at temperatures below 1.8 K were performed on single-crystals using a micro-SQUID instrument.[19]

---

(6) Eppley, H. J.; Tsai, H. L.; de Vries, N.; Folting, K.; Christou, G.; Hendrickson, D. N. *J. Am. Chem. Soc.* **1995**, *117*, 301.

(7) Soler, M.; Chandra, S. K.; Ruiz, D.; Davidson, E. R.; Hendrickson, D. N.; Christou, G. *Chem. Commun.* **2000**, 2417–2418.

(8) (a) Hendrickson, D. N.; Christou, G.; Ishimoto, H.; Yoo, J.; Brechin, E. K.; Yamaguchi, A.; Rumberberg, E. M.; Aubin, S. M. J.; Sun, Z.; Aromi, G. *Polyhedron* **2001**, *20*, 1479 and references therein. (b) Boskovic, C.; Brechin, E. K.; Streib, W. E.; Folting, K.; Bollinger, J. C.; Hendrickson, D. N.; Christou, G. *J. Am. Chem. Soc.* **2002**, 124, 3725. (c) Soler, M.; Rumberberg, E. M.; Folting, K.; Hendrickson, D. N.; Christou, G. *Polyhedron* **2001**, *20*, 1365. (d) Cadiou, C.; Murrie, M.; Paulsen, C.; Villar, V.; Wernsdorfer, W.; Winpenny, R. E. P. *Chem. Commun.* **2001**, 2666. (e) Brechin, E. K.; Soler, M.; Davidson, J.; Hendrickson, D. N.; Parsons, S.; Christou, G. *Chem. Commun.* **2002**, 2252. (f) Jones, L. F.; Brechin, E. K.; Collison, D.; Harrison, A.; Teat, S. J.; Wernsdorfer, W. *Chem. Commun.* **2002**, 2974. (g) Milios, C. J.; Raptopoulou, C. P.; Terzis, A.; Lloret, F.; Vicente, R.; Perlepes, S. P.; Escuer, A. *Angew. Chem., Int. Ed.* **2004**, *43*, 210. (h) Price, J. P.; Batten, S. R.; Moubaraki, B.; Murray, K. S. *Chem. Commun.* **2002**, 762. (i) Goodwin, J. C.; Sessoli, R.; Gatteschi, D.; Wernsdorfer, W.; Powell, A. K.; Heath, S. L. *J. Chem. Soc., Dalton Trans.* **2000**, 1835. (j) Andres, H.; Basler, R.; Blake, A. J.; Cadiou, C.; Chaboussant, G.; Grant, C. M.; Gudel, H.-U.; Murrie, M.; Parsons, S.; Paulsen, C.; Semadini, F.; Villar, V.; Wernsdorfer, W.; Winpenny, R. E. P. *Chem. Eur. J.* **2002**, *8*, 4867–4876. (k) Berlinguette, C. P.; Vaughn, D.; Canada-Vilalta, C.; Galan-Mascaras, J. R.; Dunbar, K. R. *Angew. Chem., Int. Ed.* **2003**, *42*, 1523. (l) Sokol, J. J.; Hee, A. G.; Long, J. R. *J. Am. Chem. Soc.* **2002**, *124*, 7656.

(9) Sañudo, E. C.; Wernsdorfer, W.; Abboud, K. A.; Christou, G. *Inorg. Chem.* **2004**, *43*, 4137.

(10) Soler, M.; Wernsdorfer, W.; Folting, K.; Pink, M.; Christou, G. *J. Am. Chem. Soc.* **2004**, *126*, 2156.

(11) Tasiopoulos, A.; Vinslava, A.; Wernsdorfer, W.; Abboud, K. A.; Christou, G. *Angew. Chem., Int. Ed.* **2004**, *43*, 2117.

(12) (a) Wernsdorfer, W.; Aliaga-Alcalde, N.; Hendrickson, D. N.; Christou, G. *Nature* **2002**, *416*, 406. (b) Hill, S.; Edwards, R. S.; Aliaga-Alcalde, N.; Christou, G. *Science* **2003**, *302*, 1015.

(13) Cotton, F. A.; Wilkinson, G.; *Advanced Inorganic Chemistry*, 4th ed.; John Wiley and Sons: New York, 1980,

(14) Sangregorio, C.; Ohm, T.; Paulsen, C.; Sessoli, R.; Gatteschi, D. *Phys. Rev. Lett.* **1997**, *78*, 4645.

(15) Aubin, S. M. J.; Dilley, N. R.; Pardi, L.; Krzystek, J.; Wemple, M. W.; Brunel, L. C.; Maple, M. B.; Christou, G.; Hendrickson, D. N. *J. Am. Chem. Soc.* **1998**, *120*, 4991.

(16) Aromi, G.; Aubin, S. M. J.; Bolcar, M. A.; Christou, G.; Eppley, H. J.; Folting, K.; Hendrickson, D. N.; Huffman, J. C.; Squire, R. C.; Tsai, H. L.; Wang, S.; Wemple, M. *Polyhedron* **1998**, *17*, 3005.

(17) Brechin, E. K.; Boskovic, C.; Wernsdorfer, W.; Yoo, J.; Yamaguchi, A.; Sanudo, E. C.; Concolino, T. R.; Rheingold, A. L.; Ishimoto, H.; Hendrickson, D. N.; Christou, G. *J. Am. Chem. Soc.* **2002**, *124*, 9710.

(18) Vincent, J. B; Chang, H. R.; Folting, K.; Huffman, J. C.; Christou, G.; Hendrickson, D. N. *J. Am. Chem. Soc.* **1987**, *109*, 5703.

(19) Wernsdorfer, W. *Adv. Chem. Phys.* **2001**, *118*, 99.

Table 1. Crystallographic and Structure Refinement Data for **1**·6MeCN

temp	223(2) K	β, deg	77.7478(7)
cryst syst	triclinic	γ, deg	66.4181(11)
space group	$P\bar{1}$	V, Å^3	3288.56(22)
a, Å	13.4785(3)	Z	1
b, Å	15.4119(4)	ρ_{calc}, g cm^{-3}	1.762
c, Å	17.7509(4)	R1,[a] %	13.66
α, deg	89.8405(8)	wR2,[b] %	29.82

[a] $R1 = 100\sum(||F_o| - |F_c||)/\sum|F_o|$. [b] $wR2 = [\sum[w(F_o^2 - F_c^2)^2]/\sum[w(F_o^2)^2]]^{1/2}$. $S = [\sum[w(F_o^2 - F_c^2)^2]/(n - p)]^{1/2}$, $w = 1/[\sigma^2(F_o^2) + (0.0742p)^2]$, $p = [\max(F_o^2, 0) + 2F_c^2]/3$.

Chart 1

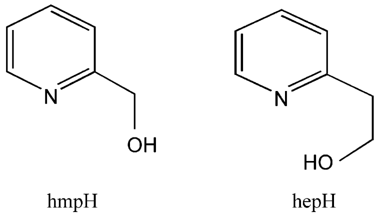

hmpH hepH

X-ray Crystallography and Structure Solution. Data were collected on a Bruker platform goniometer equipped with a SMART APEX CCD area detector and a graphite monochromator utilizing Mo Kα radiation ($\lambda = 0.71073$ Å). A suitable crystal of **1**·6MeCN was mounted on a glass fiber using silicone grease and transferred to the diffractometer where it was cooled to 223 K for characterization and data collection. The intensity data were collected using the Φ- and ω-scan methods, with a scan step $\Delta\Phi = \Delta\omega = 0.03°$. The first 50 frames were remeasured at the end of data collection to monitor instrument and crystal stability. The data were corrected for Lorentz and polarization effects using the Bruker SAINT software, and an absorption correction was performed using the DIFABS program supplied by Bruker AXS. The structure was solved by direct methods and standard Fourier techniques, and was refined on F^2 using full-matrix least-squares method (SHELXTL).[20] All non-H atoms were refined anisotropically; H-atoms were placed in calculated positions and refined with the use of a riding model. Unit cell parameters and data collection and refinement details are listed in Table 1.

Results and Discussion

Synthesis. The trinuclear Mn complex $[Mn_3O(O_2CMe)_6(py)_3](ClO_4)$ has previously been found to be useful starting material for the synthesis of new Mn−carboxylate complexes. Reactions of this complex with appropriate chelating ligands have afforded a variety of new clusters with a variety of nuclearities. Of relevance to the present work is the previously studied reaction of $[Mn_3O(O_2CMe)_6(py)_3](ClO_4)$ with 3 equiv of hydroxymethylpyridine (hmpH) in CH_2Cl_2, which was found to give the decanuclear Mn(III) complex $[Mn_{10}O_6(OH)_2(O_2CMe)_8(hmp)_8](ClO_4)_4$.[21]

The organic compounds hmpH and hepH are structurally very similar (Chart 1), only differing in an extra CH_2 group in the alcohol arm. In contrast with the results obtained with hmpH, the reaction of $[Mn_3O(O_2CMe)_6(py)_3](ClO_4)$ in MeCN with 3 equiv of hepH afforded the new mixed valent $[Mn(II)_2Mn(III)_{16}]$ complex $[Mn_{18}O_{14}(O_2CMe)_{18}(hep)_4(hepH)_2(H_2O)_2](ClO_4)_2$ (**1**). However, the yield of complex **1** was <5% and the preparation difficult to reproduce; thus, a better route to this compound was sought and subsequently developed.

Since complex **1** contains some Mn(II), indicating that the formation of this product requires some disproportionation or reduction of Mn(III) in the starting material to occur, we explored whether deliberately adding a Mn(II) source might provide a more reliable route to **1**. Thus, we investigated the reactions of hepH with a mixture of $[Mn_3O(O_2CMe)_6(py)_3](ClO_4)$ and its mixed-valence Mn(II), 2Mn(III) version, $[Mn_3O(O_2CMe)_6(py)_3]$. Indeed, the reaction of an MeCN solution of $[Mn_3O(O_2CMe)_6(py)_3](ClO_4)$ and $[Mn_3O(O_2CMe)_6(py)_3]$ in a 2:1 ratio with 1.5−3 equiv of hepH afforded **1** in a reproducible yield of 20%. This ratio of Mn_3 reagents is that calculated to give a 16Mn(III)/2Mn(II) oxidation state ratio. The overall transformation is summarized in eq 1.

$$4[Mn_3O(O_2CMe)_6(py)_3]^+ + 2[Mn_3O(O_2CMe)_6(py)_3] + 6hepH + 10H_2O \rightarrow [Mn_{18}O_{14}(O_2CMe)_{18}(hep)_4(hepH)_2(H_2O)_2]^{2+} + 18MeCO_2H + 2H^+ + 18py \quad (1)$$

The 2:1 reaction ratio of Mn_3 reagents does not require any redox processes. However, subsequent reactions exploring the effect of varying the ratio from 2:1 to 1:2 always afforded the same complex **1** as the only isolable product, although the 2:1 ratio does give the highest yield.

Description of Structure. $[Mn_{18}O_{14}(O_2CMe)_{18}(hep)_4(hepH)_2(H_2O)_2](ClO_4)_2\cdot 6MeCN$ (**1**·6MeCN) crystallizes in the triclinic space group $P\bar{1}$. Selected bond distances and angles are listed in Table 2, and an ORTEP representation and stereoview of the cation are presented in Figure 1. The structure consists of one $[Mn_{18}]^{2+}$ cation and two perchlorate anions per unit cell, with the former lying on a crystallographic inversion center. The cation of **1** can be described as disc-shaped with 10 of the metals in a nearly planar arrangement and Mn(4), Mn(7), Mn(8), and Mn(9) and their symmetry related Mn(4)′, Mn(7)′, Mn(8)′, and Mn(9)′ lying above and below the plane, as shown in Figure 2. It consists of a $[Mn_{18}(\mu_4\text{-}O)_4(\mu_3\text{-}O)_{12}(\mu_2\text{-}O)_8]^{4+}$ core (Figure 2), with the four μ_4-O atoms (O(22), O(23), O(22)′, and O(23)′) and 10 of the μ_3-O atoms (O(19), O(20), O(21), O(24), O(25), O(19)′, O(20)′, O(21)′, O(24)′, and O(25)′) atoms being O^{2-} ions. The remaining two μ_3-O atoms (O(10) and O(10)′) are from μ_4-$MeCO_2^-$ groups, an extremely rare binding mode for this ligand in molecular clusters. Of the eight μ_2-O atoms, six are part of hep/hepH ligands (O(26), O(27), O(28), O(26)′, O(27)′, and O(28)′), and the other two (O(4) and O(4)′) are from bridging *syn*,*syn*, *anti*-$MeCO_2^-$ groups. The core can be described as a central $[Mn_4O_6]$ unit (containing a linear Mn_4 chain) linked by its μ_3-O^{2-} ions to two $[Mn_7O_9]$ units, one on each side. Each of the latter comprises a face-sharing set of one $[Mn_4O_4]$ cubane and two $[Mn_3O_4]$ partial cubanes. All of the Mn centers are hexacoordinated. Peripheral ligation is provided by acetate groups and the hepH/hep$^-$ ligands.

---

(20) Sheldrick, G. M. *SHELXTL5*; Bruker-AXS: Madison, WI, 1998.
(21) Harden, N. C.; Bolcar, M. A.; Wernsdorfer, W.; Abboud, K. A.; Streib, W. E.; Christou, G. *Inorg. Chem.* **2003**, *42*, 7067.

Table 2. Selected Bond Distances (Å) and Angles (deg) for **1**·6MeCN

Mn(1)−O(25)	1.896(11)	O(25)−Mn(1)−O(21)	98.2(5)	O(25)−Mn(1)−O(25)	80.9(5)
Mn(1)−O(25)	1.897(11)	O(21)−Mn(1)−O(25)	174.6(5)	O(25)−Mn(1)−O(24)	177.8(4)
Mn(1)−O(16)	2.168(10)	O(21)−Mn(1)−O(24)	81.6(5)	O(25)−Mn(1)−O(24)	99.1(5)
Mn(2)−O(19)	1.889(11)	O(25)−Mn(1)−O(16)	89.6(4)	O(21)−Mn(1)−O(16)	92.3(4)
Mn(2)−O(23)	1.959(11)	O(25)−Mn(1)−O(16)	93.0(4)	O(24)−Mn(1)−O(16)	92.6(4)
Mn(2)−O(10)	2.312(11)	O(25)−Mn(2)−O(19)	91.7(5)	O(25)−Mn(2)−O(22)	94.6(5)
Mn(3)−O(19)	1.871(11)	O(19)−Mn(2)−O(22)	173.5(5)	O(25)−Mn(2)−O(23)	175.3(5)
Mn(3)−O(20)	1.946(11)	O(19)−Mn(2)−O(23)	86.9(5)	O(22)−Mn(2)−O(23)	86.9(5)
Mn(3)−O(10)	2.315(11)	O(25)−Mn(2)−O(4)	97.3(4)	O(19)−Mn(2)−O(4)	86.9(4)
Mn(4)−O(20)	1.908(11)	O(22)−Mn(2)−O(4)	90.6(4)	O(23)−Mn(2)−O(4)	87.1(4)
Mn(4)−O(3)	1.953(11)	O(25)−Mn(2)−O(10)	96.8(4)	O(19)−Mn(2)−O(10)	83.4(4)
Mn(4)−O(23)	2.315(11)	O(22)−Mn(2)−O(10)	97.5(4)	O(23)−Mn(2)−O(10)	78.6(4)
Mn(5)−O(24)	1.868(12)	O(4)−Mn(2)−O(10)	163.0(4)	O(21)−Mn(3)−O(19)	90.1(5)
Mn(5)−O(17)	1.944(11)	O(21)−Mn(3)−O(13)	96.7(5)	O(19)−Mn(3)−O(13)	173.2(5)
Mn(5)−O(4)	2.490(10)	O(21)−Mn(3)−O(20)	165.6(5)	O(19)−Mn(3)−O(20)	80.3(5)
Mn(6)−O(21)	1.886(12)	O(13)−Mn(3)−O(20)	93.0(5)	O(21)−Mn(3)−O(7)	95.5(5)
Mn(6)−O(14)	1.989(13)	O(19)−Mn(3)−O(7)	91.1(5)	O(13)−Mn(3)−O(7)	88.4(5)
Mn(6)−O(29)	2.321(11)	O(20)−Mn(3)−O(7)	95.3(5)	O(21)−Mn(3)−O(10)	89.9(5)
Mn(7)−O(23)	1.917(11)	O(19)−Mn(3)−O(10)	83.7(4)	O(13)−Mn(3)−O(10)	96.2(4)
Mn(7)−O(26)	1.947(12)	O(20)−Mn(3)−O(10)	78.6(4)	O(7)−Mn(3)−O(10)	172.5(5)
Mn(7)−O(22)	2.278(11)	O(19)−Mn(4)−O(20)	81.7(5)	O(19)−Mn(4)−O(11)	171.6(5)
Mn(8)−O(20)	1.884(11)	O(20)−Mn(4)−O(11)	93.2(5)	O(19)−Mn(4)−O(3)	92.1(5)
Mn(8)−N(1)	2.058(16)	O(20)−Mn(4)−O(3)	167.5(5)	O(11)−Mn(4)−O(3)	91.6(5)
Mn(8)−O(10)	2.341(12)	O(19)−Mn(4)−O(8)	93.2(5)	O(20)−Mn(4)−O(8)	94.8(5)
Mn(9)−O(6)	2.130(11)	O(11)−Mn(4)−O(8)	93.9(5)	O(3)−Mn(4)−O(8)	96.5(5)
Mn(9)−O(9)	2.170(11)	O(19)−Mn(4)−O(23)	78.0(4)	O(20)−Mn(4)−O(23)	77.6(4)
Mn(9)−O(27)	2.279(11)	O(11)−Mn(4)−O(23)	94.5(4)	O(3)−Mn(4)−O(23)	90.4(4)
Mn(1)−O(21)	1.895(13)	O(8)−Mn(4)−O(23)	169.0(5)	O(22)−Mn(5)−O(24)	91.7(5)
Mn(1)−O(24)	1.924(11)	O(22)−Mn(5)−O(28)	82.0(5)	O(24)−Mn(5)−O(28)	168.3(5)
Mn(2)−O(25)	1.850(11)	O(22)−Mn(5)−O(17)	170.2(5)	O(24)−Mn(5)−O(17)	95.6(5)
Mn(2)−O(22)	1.889(10)	O(28)−Mn(5)−O(17)	89.6(5)	O(22)−Mn(5)−O(2)	97.4(5)
Mn(2)−O(4)	2.195(11)	O(24)−Mn(5)−O(2)	98.2(5)	O(28)−Mn(5)−O(2)	92.5(5)
Mn(3)−O(21)	1.865(13)	O(17)−Mn(5)−O(2)	88.0(5)	O(22)−Mn(5)−O(4)	82.6(4)
Mn(3)−O(13)	1.954(13)	O(24)−Mn(5)−O(4)	90.5(4)	O(28)−Mn(5)−O(4)	78.9(4)
Mn(3)−O(7)	2.150(11)	O(17)−Mn(5)−O(4)	90.9(4)	O(2)−Mn(5)−O(4)	171.3(5)
Mn(4)−O(19)	1.855(11)	O(24)−Mn(6)−O(21)	83.3(5)	O(24)−Mn(6)−O(18)	96.0(5)
Mn(4)−O(11)	1.936(13)	O(21)−Mn(6)−O(18)	178.9(5)	O(24)−Mn(6)−O(14)	179.1(6)
Mn(4)−O(8)	2.121(12)	O(21)−Mn(6)−O(14)	96.2(6)	O(18)−Mn(6)−O(14)	84.5(5)
Mn(5)−O(22)	1.865(11)	O(24)−Mn(6)−O(15)	91.2(5)	O(21)−Mn(6)−O(15)	93.1(5)
Mn(5)−O(28)	1.938(13)	O(18)−Mn(6)−O(15)	87.8(5)	O(14)−Mn(6)−O(15)	89.6(6)
Mn(5)−O(2)	2.125(11)	O(24)−Mn(6)−O(29)	93.7(5)	O(21)−Mn(6)−O(29)	87.8(5)
Mn(6)−O(24)	1.868(11)	O(18)−Mn(6)−O(29)	91.4(5)	O(14)−Mn(6)−O(29)	85.5(5)
Mn(6)−O(18)	1.953(12)	O(15)−Mn(6)−O(29)	175.1(5)	O(5)−Mn(7)−O(23)	168.6(5)
Mn(6)−O(15)	2.195(12)	O(5)−Mn(7)−O(28)	93.0(5)	O(23)−Mn(7)−O(28)	96.2(5)
Mn(7)−O(5)	1.910(11)	O(5)−Mn(7)−O(26)	93.1(5)	O(23)−Mn(7)−O(26)	77.8(5)
Mn(7)−O(28)	1.925(12)	O(28)−Mn(7)−O(26)	173.8(5)	O(5)−Mn(7)−N(3)	88.9(5)
Mn(7)−N(3)	2.266(16)	O(23)−Mn(7)−N(3)	98.1(5)	O(28)−Mn(7)−N(3)	88.1(6)
Mn(8)−O(23)	1.876(12)	O(26)−Mn(7)−N(3)	91.2(6)	O(5)−Mn(7)−O(22)	98.8(5)
Mn(8)−O(26)	1.888(11)	O(23)−Mn(7)−O(22)	77.7(4)	O(28)−Mn(7)−O(22)	72.3(5)
Mn(8)−O(12)	2.135(13)	O(26)−Mn(7)−O(22)	107.5(5)	N(3)−Mn(7)−O(22)	159.2(5)
Mn(9)−O(22)	2.132(11)	O(23)−Mn(8)−O(20)	90.4(5)	O(23)−Mn(8)−O(26)	80.3(5)
Mn(9)−O(1)	2.147(11)	O(20)−Mn(8)−O(26)	167.2(5)	O(23)−Mn(8)−N(1)	172.0(5)
Mn(9)−N(2)	2.264(15)	O(20)−Mn(8)−N(1)	96.9(5)	O(26)−Mn(8)−N(1)	92.0(5)
		O(23)−Mn(8)−O(12)	93.5(5)	O(20)−Mn(8)−O(12)	89.3(5)
		O(26)−Mn(8)−O(12)	99.9(5)	N(1)−Mn(8)−O(12)	90.1(6)
		O(23)−Mn(8)−O(10)	79.4(4)	O(20)−Mn(8)−O(10)	79.1(4)
		O(26)−Mn(8)−O(10)	90.5(5)	N(1)−Mn(8)−O(10)	98.5(5)
		O(12)−Mn(8)−O(10)	166.2(4)	O(22)−Mn(9)−O(6)	88.8(4)
		O(22)−Mn(9)−O(1)	97.2(4)	O(6)−Mn(9)−O(1)	88.7(5)
		O(22)−Mn(9)−O(9)	90.2(4)	O(6)−Mn(9)−O(9)	92.8(5)
		O(1)−Mn(9)−O(9)	172.5(5)	O(22)−Mn(9)−N(2)	167.5(5)
		O(6)−Mn(9)−N(2)	87.2(5)	O(1)−Mn(9)−N(2)	94.6(5)
		O(9)−Mn(9)−N(2)	78.2(5)	O(22)−Mn(9)−O(27)	102.4(4)
		O(6)−Mn(9)−O(27)	168.8(4)	O(1)−Mn(9)−O(27)	90.7(4)
		O(9)−Mn(9)−O(27)	86.4(4)	N(2)−Mn(9)−O(27)	81.7(5)

Close examination of the metric parameters (Table 2) and bond valence sum calculations[22] for the Mn atoms (Table 3) reveals a mixed- and trapped-valence oxidation state description of 16 Mn(III) and 2 Mn(II) centers. The two Mn(II) ions are Mn(9) and Mn(9)′. Bond valence sum calculations were also performed on the oxygen atoms[23,24] of the cluster to identify their protonation level (Table 4), and this revealed two terminal water molecules, O(29) and O(29)′, and two protonated hepH ligands, O(27) and O(27)′.

---

(22) Liu, W.; Thorp, H. H. *Inorg. Chem.* **1993**, *32*, 4102.

(23) Brown, I. D.; Shannon, R. D. *Acta Crystallogr.* **1973**, *A29*, 266.

(24) Donnay, G.; Allman, R. *Am. Mineral.* **1970**, *55*, 1003.

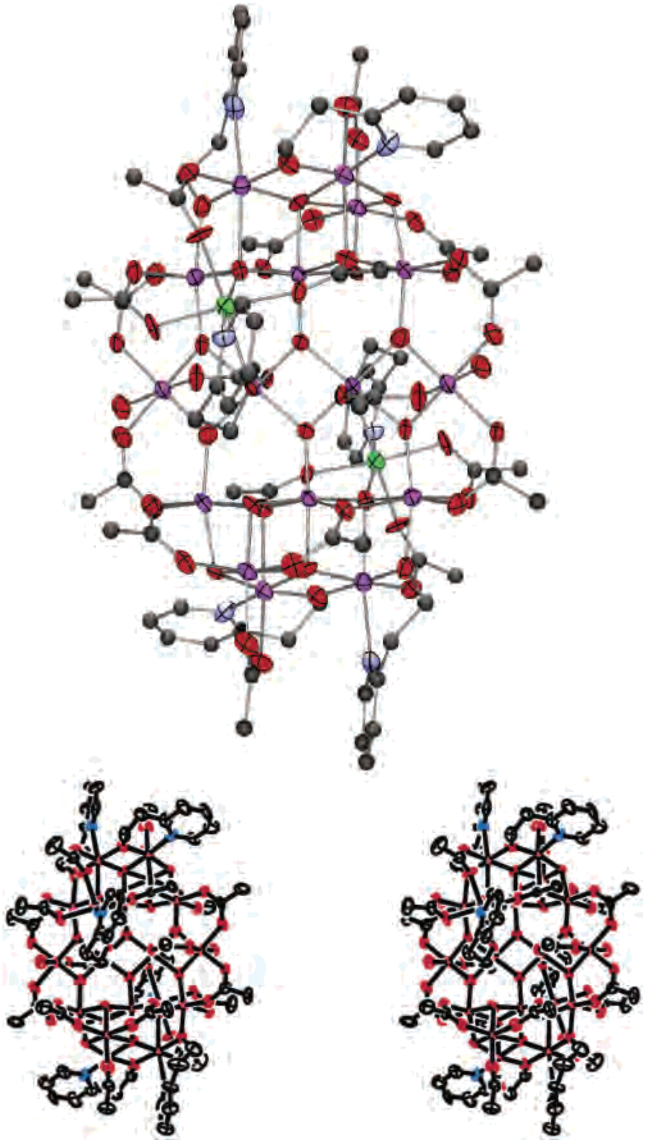

Figure 1. ORTEP plot at the 50% probability level of the cation of **1**. Color code: purple Mn(III), green Mn(II), red O, blue N, black C.

These determined protonation levels and metal oxidation states are consistent with an overall $[Mn_{18}]^{2+}$ charge for the cation of **1**, as revealed by the two ClO_4^- anions in the crystal structure.

All the Mn(III) atoms show the expected Jahn−Teller (JT) distortion of high-spin Mn(III) in near-octahedral geometry, and this takes the form of an axial elongation in every case. Ten of the metal centers (Mn(1), Mn(2), Mn(3), Mn(5), Mn(6), and their symmetry partners) are coplanar, with their JT elongation axes aligned approximately parallel to each other and perpendicular to the plane, as shown in Figure 2 (bottom). The remaining six Mn(III) atoms (Mn(4), Mn(7), Mn(8), and their symmetry partners) lie above and below this plane: the JT axes on Mn(7), Mn(8), Mn(7)′, and Mn(8)′ lie approximately parallel to the plane of the molecule, and thus are essentially perpendicular to the majority JT orientations, whereas those on Mn(4) and Mn(4)′ are at an intermediate orientation. This will be of relevance to the magnetic properties to be discussed below.

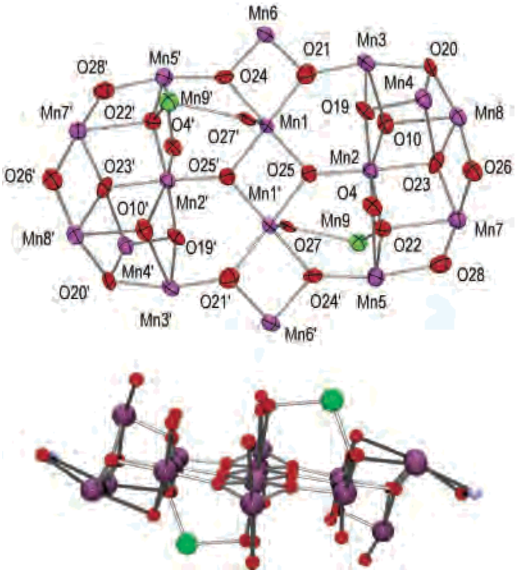

Figure 2. (top) Labeled ORTEP plot of the core of the cation of **1**, from a viewpoint approximately perpendicular to the molecular plane. (bottom) PovRay plot approximately along the molecular plane showing the Mn(III) JT elongation axes as thicker black bonds. Color code: purple Mn(III), green Mn(II), red O, blue N, black C.

Table 3. Bond Valence Sums[a] for the Mn Atoms in **1**

	Mn(II)	Mn(III)	Mn(IV)
Mn(1)	3.166	$\underline{2.896}$	3.040
Mn(2)	3.358	$\underline{3.071}$	3.224
Mn(3)	3.306	$\underline{3.024}$	3.175
Mn(4)	3.303	$\underline{3.021}$	3.172
Mn(5)	3.282	$\underline{3.001}$	3.151
Mn(6)	3.158	$\underline{2.888}$	3.032
Mn(7)	3.177	$\underline{2.923}$	3.041
Mn(8)	3.334	$\underline{3.079}$	3.184
Mn(9)	$\underline{2.010}$	1.856	1.921

[a] The underlined value is the one closest to the charge for which it was calculated. The oxidation state of a particular atom can be taken as the nearest whole number to the underlined value.

Table 4. Bond Valence Sums for Selected Oxygen Atoms in **1**[a]

atom	BVS	assignment	group
O(29)	0.199	H_2O	H_2O
O(27)	1.181	ROH	hepH
O(26)	2.061	RO^-	hep^-
O(28)	2.094	RO^-	hep^-

[a] The O atom is not protonated if the BVS is ∼2, it is monoprotonated if the BVS is ∼1, and it is doubly protonated if the BVS is ∼0.

The Mn_{18} cations in the triclinic $P\bar{1}$ lattice are stacked in columns, and all of the molecules are oriented in the same way with respect to the cell axes. Between molecules in the same column, there is no evidence of hydrogen-bonding or any other close contact. Between columns there are narrow channels filled with MeCN solvent molecules, which are disordered due to insignificant interaction with any of the anions or cations around them. The only significant intermolecular interaction is π-stacking of the hep^- pyridine rings bound to Mn(8) atoms in $[Mn_{18}]^{2+}$ cations in different columns along the *c*-direction of the cell; this is shown in Figure 3 as dashed lines. The aromatic rings are perfectly parallel and separated by 3.7 Å. Thus, apart from this π-stacking, each cation is fairly isolated from its neighbors

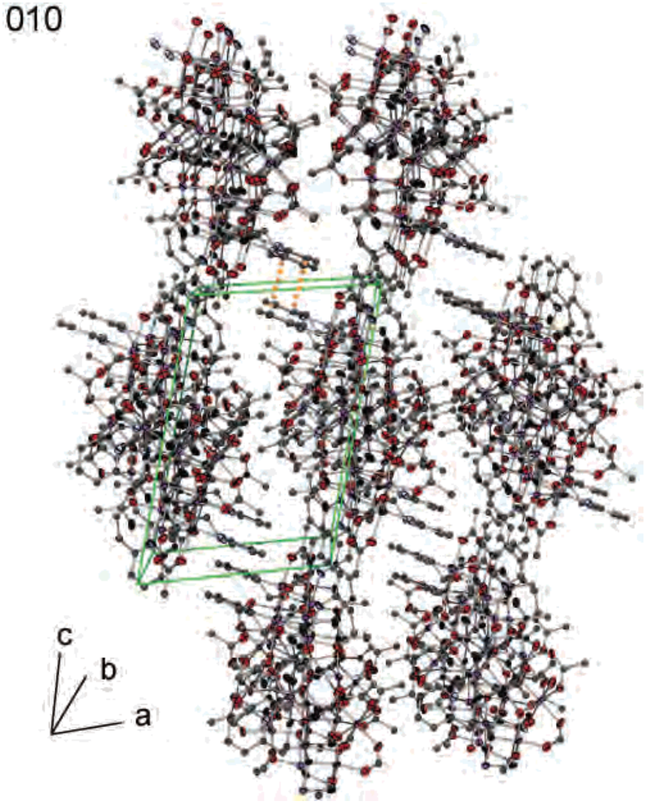

Figure 3. Packing diagram of **1**. A representative pair of π-stacking aromatic rings of hep$^-$ ligands is indicated by the dashed lines.

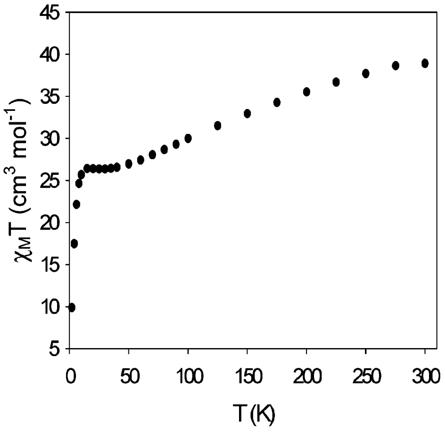

Figure 4. Direct current magnetic susceptibility plot for **1** in a 1.0 T magnetic field.

in the crystal. This fact will also be important when interpreting the magnetic properties of the complexes.

Direct Current Magnetic Susceptibility Studies. Direct current magnetic susceptibility studies were performed on a microcrystalline sample of complex **1** in the 5.0−300 K range and a 1 T applied field. Figure 4 shows the molar magnetic susceptibility (χ_M) of complex **1** as a $\chi_M T$ versus T plot. The $\chi_M T$ has a value of 38.9 cm^3 K mol^{-1} at 300 K, gradually decreasing with decreasing temperature to a plateau value of 26.4 cm^3 K mol^{-1} between 40 and 15 K, and then sharply decreasing to 9.8 cm^3 K mol^{-1} at 5.0 K. The $\chi_M T$ value at 300 K is significantly smaller than the spin-only value of 56.75 cm^3 K mol^{-1} expected for 18 noninteracting Mn centers with the oxidation states found in complex **1**.

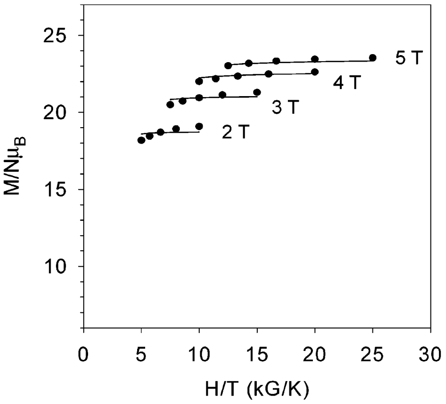

Figure 5. Plot of reduced magnetization ($M/N\mu_B$) vs H/T for **1** at the indicated applied fields and temperatures in the 2.0−4.0 K range. The lines are the best fit to the experimental data (see the text for the fit parameters).

These dc data are thus consistent with predominantly antiferromagnetic interactions between the metal centers, but with a relatively large ground-state spin. To determine the exact values of the many pairwise Mn_2 exchange parameters and to find all of the possible spin states and their energies, the spin Hamiltonian for this complex would have to be diagonalized.[25] However, such a matrix-diagonalization approach would involve a matrix of dimensions of 549×10^{10} by 549×10^{10}, and such a calculation is essentially unfeasible with current computing capabilities. It is also not possible, due to the complexity of the system, to apply the equivalent operator approach, based on the Kambe vector coupling method,[26] as is usually possible with smaller systems. Thus, we concentrated instead on identifying only the ground-state spin (S) of the complex, which would in any case dominate the very low-temperature magnetic studies to be discussed later.

Variable-temperature, variable-field dc magnetization (M) data were collected in the 2.0−4.0 K range at applied dc fields (H) ranging from 2.0 to 5.0 T. The obtained data are plotted as reduced magnetization ($M/N\mu_B$) versus H/T in Figure 5. The data were fit by diagonalization of the spin Hamiltonian matrix using a full powder-average method that assumes only the ground state is populated and incorporates axial ZFS ($D\hat{S}_z^2$) and Zeeman effects. The method is described in detail elsewhere.[9,27] The best fit gave a ground-state spin of $S = 13$, $D = -0.13$ cm^{-1} (-0.18 K) and $g = 1.86$, and is shown in Figure 5 as the solid lines. If data collected at lower fields were included, a good fit could not be obtained. This is indicative of the presence of low-lying excited states, as expected (i) for such a high nuclearity cluster, which will consequently have a high density of spin states, and (ii) for a molecule containing Mn(II) ion, since these display weak exchange interactions, and consequently small energy separations between spin states.

However, what is not clear from these data and fit by themselves is whether the $S = 13$ state is the ground state, or whether it is one of the lowest-lying excited states above

---

(25) Kahn, O. *Molecular Magnetism*; VCH: New York, 1993.

(26) Kambe, K. *J. Phys. Soc. Jpn.* **1950**, *5*, 48.

(27) Eppley, H. J.; Tsai, H.-L.; De Vries, N.; Folting, K.; Christou, G.; Hendrickson, D. N. *J. Am. Chem. Soc.* **1995**, *117*, 301.

a ground state with an $S < 13$ spin. In the latter case, the M_S component of the $S = 13$ excited state would cross below those of the ground state in large fields, and the magnetization fits would thus appear to indicate an $S = 13$ ground state, which would not be the true case. Such an incorrect determination of the ground state spin is always a danger when low-lying excited states are present and a large dc field is employed, and we have elsewhere described how we avoid this by using only weak dc fields to avoid level crossings in cases where the low-lying excited states have a bigger spin than the ground state.[9,10] In the present case, however, the in-phase ac susceptibility studies (which will be described below), carried out in an oscillating ac field of only 3.5 G, serve to indicate that the $S = 13$ state really is the ground state of the molecule, with the low-lying excited states having smaller S. Thus, the use of large dc fields provides data and subsequent fit values of S and D that are not an artifact of level crossing, and thus reliable.

The obtained D value is relatively small compared with other Mn complexes such as $[Mn_{12}O_{12}(O_2CMe)_{16}(H_2O)_4]$ ($D = -0.5$ cm^{-1} $= -0.71$ K),[1-3] even though the molecule possesses 16 Mn(III) instead of only eight of them as in $[Mn_{12}O_{12}(O_2CMe)_{16}(H_2O)_4]$. This can be rationalized as reflecting the difference in the relative orientations of the Mn(III) JT axes in the two types of molecule. The JT distorted Mn(III) ions are the main source of the molecular anisotropy (i.e., the magnitude of the molecular zero-field splitting parameter, D), which is a projection of the Mn(III) single-ion anisotropies onto the molecular anisotropy (z) axis. In the Mn_{12} complex, the eight Mn(III) JT axes are very roughly all parallel leading to a much larger $|D|$ value than for the cation of **1**, which has 10 JT axes roughly parallel, but with four of the remaining six perpendicular to them and the other two in an intermediate orientation. As a result, it is qualitatively reasonable that the D value for **1** should be smaller (less negative) than that for the Mn_{12} clusters.

Even though higher spin values are known, the $S = 13$ ground-state spin of complex **1** is nevertheless an unusually large spin for a molecular species. The currently largest spin for any molecular species is the $S = {}^{51}/_2$ of a Mn_{25} complex,[28] and a Mo_6Mn_9 complex.[29] As mentioned in the Introduction, the upper limit to the barrier to magnetization reversal is given by $U = S^2|D|$ for an integer spin system, although the actual or effective barrier (U_{eff}) is significantly less due to quantum tunneling of the magnetization (QTM) through the barrier via higher energy M_S levels. The large $S = 13$ spin is beneficial for providing a large barrier, but the small D value counterbalances this, and the calculated U value is consequently only 22.0 cm^{-1} (=31.6 K). In contrast, a D value of -0.5 cm^{-1}, as for the Mn_{12} complex, would have given a U of 84.5 cm^{-1} for $S = 13$. Nevertheless, a value of $U = 22.0$ cm^{-1} is sufficiently large to suggest that, at a low enough temperature, complex **1** might function as an SMM.

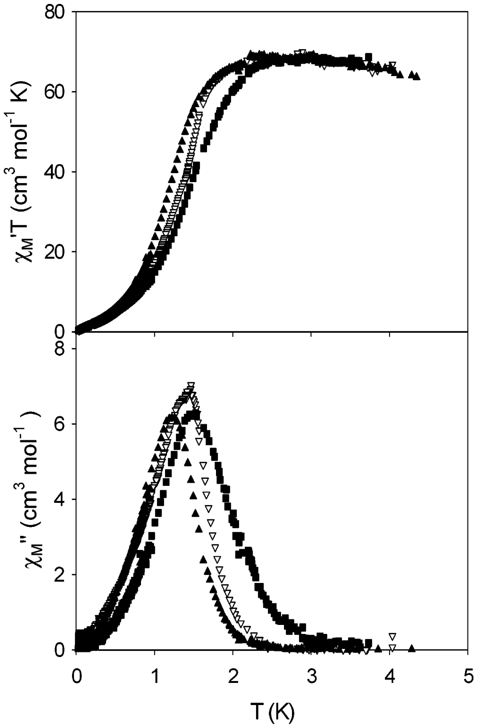

Figure 6. Alternating magnetic susceptibility plot for **1** at 44 (■), 246 (▽), and 996 (▲) Hz ac frequencies.

We thus decided to investigate the magnetization dynamics of this complex using ac magnetic susceptibility studies.

Alternating Current Magnetic Susceptibility Studies. In an ac susceptibility experiment, a weak field (typically 1−5 G) oscillating at a particular frequency (ν) is applied to a sample to probe the dynamics of the magnetization (magnetic moment) relaxation. Alternating current susceptibility data were collected on a microcrystalline sample of **1** in the 0.04−4.0 K range at nine frequencies from 1.1 to 996 Hz. Both the resulting in-phase (χ_M', plotted as $\chi_M'T$) and the out-of-phase (χ_M'') ac susceptibility data are shown in Figure 6. If the magnetization vector can relax fast enough to keep up with the oscillating field, then there is no out-of-phase susceptibility signal (χ_M''), and the in-phase susceptibility (χ_M') is equal to the dc susceptibility. However, if the barrier to magnetization relaxation is significant compared to thermal energy (kT), then there is a nonzero χ_M'' signal and the in-phase signal decreases. In addition, the χ_M'' signal will be frequency-dependent. As can be seen in Figure 6, a frequency-dependent χ_M'' signal begins to appear at below 3 K, concomitant with a frequency-dependent decrease in the $\chi_M'T$ signal. Such frequency-dependent ac signals are a characteristic signature of the superparamagnet-like slow relaxation of an SMM, although they do not by themselves prove the presence of an SMM.

The $\chi_M'T$ data also provide crucial support for the conclusion from the dc magnetization fits described earlier that complex **1** possesses an $S = 13$ ground state. As can be seen in Figure 5, the $\chi_M'T$ value above 3 K is increasing with decreasing temperature. A well isolated ground state (vs kT) would be expected to be essentially 100% populated at these temperatures, and thus, the $\chi_M'T$ value would be

---

(28) Murugesu, M.; Habrych, M.; Wernsdorfer, W.; Abboud, K. A.; Christou, G. *J. Am. Chem. Soc.* **2004**, *126*, 4766.

(29) Larionova, J.; Gross, M.; Pilkington, M.; Andres, H.; Stoeckli-Evans, H.; Güdel, H.; Decurtins, S. *Angew. Chem., Int. Ed.* **2000**, *39*, 1605.

expected to be essentially temperature-independent. A sloping $\chi_M'T$ versus T plot is indicative of low-lying excited states whose changing population with temperature affects the observed $\chi_M'T$. In several cases, we have observed that the $\chi_M'T$ value decreases significantly with decreasing T, and this is consistent with low-lying excited states with S values greater than that of the ground state. As they become depopulated with decreasing T, the $\chi_M'T$ value approaches that corresponding to 100% population of the ground state. For complex **1**, however, the $\chi_M'T$ is increasing with decreasing T, suggesting that those low-lying excited states populated at these temperatures have a smaller S value than the ground state. Thus, as they become depopulated, the $\chi_M'T$ value increases to that of the ground state. Extrapolation of the $\chi_M'T$ plot to 0 K gives a value of $\sim$79 cm^3 K mol^{-1}, which is consistent with $S = 13$ and $g = 1.86$, in satisfying agreement with the fit of the magnetization data. The in-phase value of $\sim$79 cm^3 K mol^{-1} is also consistent with $S = 14$ and $g = 1.73$, and $S = 12$ and $g = 2.01$, which are less favored because of the g values but nevertheless reasonable, and so the safest conclusion from the in-phase ac data alone is that complex **1** has an $S = 13 \pm 1$ ground state. However, even this is enough to allow us to rationalize the described problems with the dc magnetization fits at lower fields. At lower fields, some of the excited states will be populated even at the lowest temperatures, and this will give a poor fit since the fitting model assumes only the ground state is populated. At higher fields, however, the energy gap between the lowest-lying M_S components of the ground state and M_S levels of excited states will be greatly increased, and essentially only the former will be populated, allowing a good fit and reliable determination of the ground-state S. We thus conclude that the fit of Figure 5 is indeed reflecting the ground state, that the obtained fit parameters are reliable, and that complex **1** thus possesses an $S = 13$ ground state.

Magnetization Hysteresis Studies. With the combined dc and ac susceptibility studies revealing that complex **1** has an $S = 13$ ground state and $D = -0.13$ cm^{-1}, and exhibits out-of-phase ac susceptibility signals suggestive of a single-molecule magnet, we sought to confirm whether **1** is an SMM by determining whether it exhibits hysteresis in magnetization (M) versus dc field sweeps, the diagnostic property of a magnetic material.

Magnetization versus applied dc field data were collected on single crystals (that had been kept in contact with mother liquor) using a micro-SQUID instrument. The magnetization responses with the field approximately along the easy axis (z-axis) of the molecule are shown in Figure 7, where both the temperature dependence at a constant field sweep rate of 0.07 T/s (Figure 7, top) and the field sweep rate dependence at a constant temperature of 0.04 K (Figure 7, bottom) are shown. Hysteresis loops were indeed observed below $\sim$1 K, whose coercivities increase with decreasing temperature and increasing sweep rate, as expected for the superparamagnet-like properties of a SMM below its blocking temperature (T_B). The data thus indicate complex **1** to be a new addition to the family of SMMs. The blocking temperature (T_B) is $\sim$1.0 K, above which there is no hysteresis, i.e., the spin relaxes faster to equilibrium than the time scale of the hysteresis loop measurement.

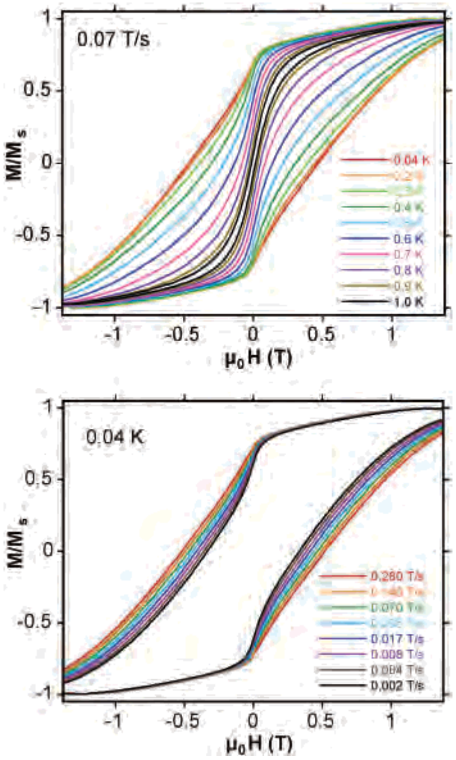

Figure 7. Magnetization (M) vs field (H) hysteresis loops for a single crystal of **1**·6MeCN at (top) a constant scan rate of 0.07 T/s and the indicated temperatures, and (bottom) at 0.7 K and the indicated scan rates. The magnetization is normalized to its saturation value M_S.

For several other SMMs studied to date, the hysteresis loops have not been smooth but have instead displayed steplike features at periodic field values.[30] These steps correspond to positions of increased magnetization relaxation rates and are due to quantum tunneling of the magnetization (QTM) through the anisotropy energy barrier.[19] The loops in Figure 7 do not show such periodic steps, although there does appear to be one barely visible at zero field. It was suspected that complex **1**·6MeCN does in fact exhibit QTM but that the steps have been broadened to the point that they have been smeared out and thus not visible. Similar behavior has been observed for certain other SMMs such as Mn$_{21}$,[9] Mn$_{30}$,[10] and Mn$_{84}$[11] species, and this has been assigned to a distribution of energy relaxation barriers (i.e., a distribution in D values) due to a distribution in local molecular environments. The separation between steps is directly proportional to D, so a distribution in D would give a distribution in step positions and thus a broadening. Such a distribution is consistent with the crystallographic disorder observed in the MeCN molecules in the crystal lattice. In

---

(30) (a) Friedman, J. R.; Sarachik, M. P.; Tejada, J.; Maciejewski, J.; Ziolo, R. *J. Appl. Phys.* **1996**, *79*, 6031. (b) Sangregorio, C.; Ohm, T.; Paulsen, C.; Sessoli, R.; Gatteschi, D. *Phys. Rev. Lett.* **1997**, *78*, 4645. (c) Aubin, S. M. J.; Dilley, N. R.; Pardi, L.; Krzystek, J.; Wemple, M. W.; Brunel, L. C.; Maple, M. B.; Christou, G.; Hendrickson, D. N. *J. Am. Chem. Soc.* **1998**, *120*, 4991. (d) Brechin, E. K.; Soler, M.; Christou, G.; Helliwell, M.; Teat, S. J.; Wernsdorfer, W. *Chem. Commun.* **2003**, 1276.

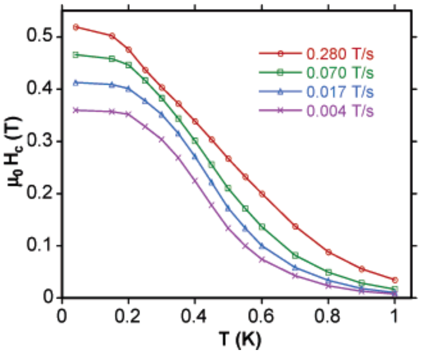

Figure 8. Plot of coercive field (H_c) vs T for a single crystal of complex **1**·6MeCN at the indicated field sweep rates.

effect, the local environments around the $[Mn_{18}]^{2+}$ cations vary as a result of these disorders, altering the value of D. Disorder in the solvent molecules was also present in the Mn_{30} and Mn_{84} SMMs that also did not display steps in their hysteresis loops. Such observations continue to emphasize the sensitivity of SMMs to relatively small changes in the local environments of the molecules. Other sources of step broadening that probably contribute to the absence of steps in Figure 7 include intermolecular dipolar and exchange interactions, particularly given the large spin of the cation of **1** and the π-stacking interactions between cations seen in the crystal structure, and of course crystal impurity and defect sites.

Although steps are not clearly visible in the hysteresis loops, they nevertheless provide other evidence of QTM. Below 0.2 K, the loops become temperature independent, but a scan rate study shows that the loops are still time-dependent (Figure 7). This is better illustrated in Figure 8, where the coercive field (half the width of the hysteresis loop at $M/M_S = 0$) is plotted as a function of temperature for different field scan rates. Below ~0.2 K, the coercive field is temperature-independent (a plateau) at a given scan rate, but scan-rate (i.e., time)-dependent at a given T. This is supportive of QTM from the ground-state $M_S = -13$ of the $S = 13$ spin manifold to $M_S < 13$ levels on the other side of the potential energy double well.

An alternative way of assessing whether QTM is occurring is to identify the presence of temperature-independent relaxation. For this, we constructed an Arrhenius plot. The ac data in Figure 6 are one source of kinetic data, since at the temperature of the peak maximum of the χ_M'' signal, the relaxation rate ($1/\tau$, where τ is the relaxation lifetime) is equal to the angular frequency ω ($=2\pi\nu$, where ν is the ac field oscillation frequency).[31] To supplement these data, dc magnetization decay data were collected: (i) on a polycrystalline sample using a SHE-RLM bridge where a SQUID serves as a null detector (a field of 3.7 G was applied, and after temperature equilibration, the field was removed and the magnetization measured as a function of time at 11 temperatures in the 0.910−0.080 K range, with data collection times up to 10^5 s at 0.080 K), and (ii) on a single-crystal at 16 temperatures in the 0.040−1.00 K range using a micro-SQUID instrument (Figure 9, top). Each of the 27 data sets was analyzed to give a relaxation time (τ). The dc decay and ac χ_M data were combined and used to construct an Arrhenius plot of ln τ versus $1/T$ (Figure 9, bottom), based on the Arrhenius relationship of eq 2, where $1/\tau_0$ is the pre-exponential factor (attempt frequency), U_{eff} is the mean effective barrier to relaxation, and k is the Boltzmann constant.

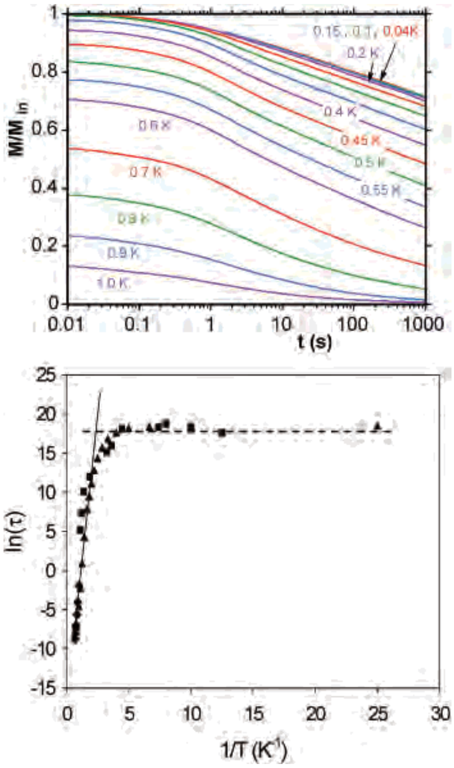

Figure 9. (top) Magnetization vs time decay plots for a single crystal of **1**·6MeCN measured on a micro-SQUID apparatus, and (bottom) Arrhenius plot for **1** using ac magnetic susceptibility data collected on a microcrystalline sample (◆), dc decay data collected on a microcrystalline sample (■), and dc decay data collected on a single crystal (▲). The solid line is the best fit to the Arrhenius equation in the thermally activated region, and the dashed line is the fit of the temperature-independent data. See the text for the fit parameters.

$$(1/\tau) = (1/\tau_0)\exp(-U_{eff}/kT) \qquad (2)$$

The fit of the thermally activated region above ~0.5 K (shown as the solid line in Figure 9, bottom) gave $U_{eff} = 14.8$ cm^{-1} $= 21.3$ K, which is less than the value of $U = S^2|D| = 22.0$ cm^{-1} $= 31.6$ K determined from the magnetization fits. This is as expected for QTM between higher energy M_S levels of the $S = 13$ manifold; i.e., the system does not have to get to the top of the barrier (i.e., the $M_S = 0$ level), but instead can tunnel through the barrier from some lower M_S level. The presence of QTM is further supported by the temperature-independence of the relaxation rate below ~0.25 K, at ~1.3×10^{-8} s^{-1}, indicative at these temperatures of QTM only between the lowest energy $M_S = \pm 13$ levels of the $S = 13$ state, i.e., ground-state tunneling. In fact, complex **1** is to date the largest spin molecule reported to display QTM.

---

[31] http://www.qdusa.com/resources/pdf/1078-201.pdf.

Conclusions

The use of hepH as a chelating ligand in Mn/O chemistry has allowed access to a structurally novel $[Mn_{18}]^{2+}$ compound, which is mixed- and trapped-valence 16Mn(III), 2Mn(II). This emphasizes the usefulness of the alkoxide functionality in promoting high-nuclearity product formation. Combined dc and ac magnetic susceptibility studies have established an unusually large ground-state spin of $S = 13$ for this compound. Together with a small but significant anisotropy, this large spin results in complex **1** being a new member of the family of SMMs, and one with a distinctly different type of structure from previous examples. The SMM property has been confirmed by hysteresis studies. The small barrier to magnetization relaxation again emphasizes the importance of both a significant S and D in producing SMMs with large relaxation barriers. Unfortunately, it is difficult to design high-nuclearity complexes to have one, let alone both, of these properties. With this new structural type of SMM established, however, we have since managed to make additional members of this Mn_{18} family of SMMs at other oxidation levels, and this work will be reported in due course. Finally, as already mentioned, complex **1** is the largest spin SMM reported to date to exhibit QTM; the largest size molecules to exhibit QTM are the recently reported Mn_{30}[10] SMM and the giant Mn_{84} SMM with a toroidal structure.[11]

Acknowledgment. This work was supported by the National Science Foundation.

Supporting Information Available: X-ray crystallographic files in CIF format for complex **1**·6MeCN. This material is available free of charge via the Internet at http://pubs.acs.org.

IC048857A